INORGANIC CHEMISTRY FRONTIERS

CCS 中国化学会 CHINESE CHEMICAL SOCIETY

ROYAL SOCIETY OF CHEMISTRY

Simultaneous Enhancement of Near Infrared Luminescence and Stability of Cs2AgInCl6:Cr3+ Double Perovskites Single Crystal Enabled by Yb3+ Dopant

Journal:	*Inorganic Chemistry Frontiers*
Manuscript ID	QI-RES-05-2022-001104.R1
Article Type:	Research Article
Date Submitted by the Author:	10-Jul-2022
Complete List of Authors:	Chen, Daiwen; Guangxi University Zhang, Xinguo; Southern Medical University, Wei, Jianwu; Guangxi University Zhou, Liya; Guangxi University, School of Chemistry and Chemical Engineering Chen, Peican; Guangxi University Pang, Qi; Guangxi University, Zhang, Jin Zhong; University of California, Santa Cruz, Department of Chemistry & Biochemistry

Simultaneous Enhancement of Near Infrared Luminescence and Stability of $Cs_2AgInCl_6:Cr^{3+}$ Double Perovskites Single Crystal Enabled by Yb^{3+} Dopant

Daiwen Chen[a], Xinguo Zhang[b], Jianwu Wei[a], Liya Zhou[a], Peican Chen[a], Qi Pang[a], and Jin Zhong Zhang[c]**

[a] *School of Chemistry and Chemical Engineering, Guangxi University /Key Laboratory of Electrochemical Energy Materials, Guangxi University, Nanning 530004, Guangxi, Peoples R China*

[b] *School of Pharmaceutical Sciences, Southern Medical University, Guangzhou 510515, Peoples R China*

[c] *Department of Chemistry and Biochemistry, University of California, Santa Cruz, California 95064, United States*

Corresponding authors: pqigx@163.com; zhang@ucsc.edu

Abstract

Broadband near infrared (NIR) emission materials are of interest for various applications including non-destructive biomedical imaging. In this work, ytterbium ion (Yb^{3+}) were successfully doped into $Cs_2AgInCl_6:Cr^{3+}$ (CAIC:Cr^{3+}) double perovskites single crystals (DPSCs) by a facile hydrothermal method. Under 365 nm excitation, the co-doped CAIC:Cr^{3+},Yb^{3+} DPSCs show broad NIR emission ranging from 800 to 1400 nm, which spans the NIR-Ⅰ (700-900 nm) and NIR-Ⅱ (1000-1700 nm) bio-windows, with a emission band at 1000 nm and a full-width at half maximum (FWHM) of 188 nm. It is found that Yb^{3+} ions doping could effectively improve the photoluminescence (PL) performance of CAIC:Cr^{3+} DPSCs. Compared to the photoluminescence quantum yield (PLQY) of 22.5% for the single doped CAIC:Cr^{3+}, the co-doped CAIC:Cr^{3+},Yb^{3+}

DPSCs show a higher PLQY of ~45%, which is attributed to the synergistic effect of reduced non-radiative recombination due to defect passivation and increase in crystallinity, and energy transfer (ET) of self-trapped excitons (STEs) to Cr^{3+}. As a demonstration of applications, NIR pc-LEDs were fabricated by combining as-synthesized NIR-emitting phosphor CAIC:Cr^{3+},Yb^{3+} with InGaN UV chips (λ_{em}=365 nm) and used to image veins in a palm and for night vision using a NIR camera. The results suggest that the synthesized CAIC: Cr^{3+},Yb^{3+} DPSCs have great potential in biological applications.

1. Introduction

High efficiency broadband near infrared (NIR) light emitters are of strong interest for applications such as night vision and biomedical imaging due to its deep penetration of biological tissues and low damage to the human body.[1, 2] Lead halide perovskites ($APbX_3$, A = Cs, CH_3NH_3, X = Cl, Br, I) have demonstrated promising applications in solar cells, photodetectors, light emitting diodes (LEDs), and other optoelectronic applications due to their superior photoelectric properties.[3-5] However, they face obstacles for commercialization due to the toxicity of lead (Pb) and low stability against humidity, oxygen and light.[4-6] For this reason, low toxicity and high stability lead-free perovskite materials have attracted substantial attention.[7] One strategy is to replace every two Pb toxicity cations with one monovalent cation and one trivalent cation, forming the double perovskites (DPs) with the general formula $A_2B(I)B(III)X_6$.[8-15] $Cs_2AgInCl_6$ as one of the direct bandgap DPs with an optical bandgap ($E_{g\ OPT}$) of ~3.3 eV has attracted much attention recently. Pure and modified $Cs_2AgInCl_6$ with excellent moisture, light and heat stability offers a promising alternative to Pb-based halide perovskites. Previous research on luminescence of DPs have mainly focused on visible light emission. Mahor *et al*. firstly obtained NIR phosphor via doping Yb^{3+} ions into $Cs_2AgInCl_6$. Nag *et al*. reported the $Cs_2AgInCl_6$ system co-doped with Bi and Er. Under 370 nm excitation, the emission intensity of the co-doped sample at 1540 nm was 45 times higher than the one of Er^{3+} doped.[16, 17] However, these research all focus on narrowband NIR emission and PLQY still needs improvement. Therefore, exploring suitable strategies for broadband NIR emission and enhance PLQY is urgently needed.

Recently, there has been growing interest in novel phosphors doped with transition metal ions or trivalent lanthanide (Ln^{3+}) ions.[18] For instance, the luminescence properties of the $^4T_2$ and ^2E energy levels in Cr^{3+} are completely different since the emission spectrum of Cr^{3+} in the six-coordinated sites is determined by the crystal field strength that is sensitive to local coordination environment.[19] Cr^{3+} can produce broadband NIR emission in the range of 650–1350 nm when located in a weak octahedral. Coordination crystal field making it the first choice for broadband NIR luminescence activators.[2,20-22]. Lanthanide (Ln) group metal cations have been found to boost photovoltaic performance of perovskite solar cells by passivating uncoordinated halide ions and improving stability.[23-25] Especially, Yb^{3+} ions can emit at around 900–1000 nm and are considered as ideal spectral converters. Inspired by the possible energy transfer between Cr^{3+} and Yb^{3+} ions, as well as the closed effective ion radius of Yb^{3+} (0.87 A˚ when CN = 6) to In^{3+} (0.80 A˚ when CN = 6), Cr^{3+} and Yb^{3+} co-doped phosphors were developed to further improve its application potential.[26] Therefore, introducing Cr^{3+} and Yb^{3+} into $Cs_2AgInCl_6$ is a promising approach to develop new NIR emitting phosphors with the characteristics of broad emission and a high PLQY.

In this work, we synthesized an efficient Cr^{3+} and Yb^{3+} co-doped CAIC DPSCs NIR-emitting phosphor by a facile hydrothermal method. The crystal structure of CAIC, CAIC:Cr^{3+} and CAIC:Cr^{3+},Yb^{3+} DPSCs was determined by X-ray diffraction (XRD) while the morphology was characterized by scan electron microscopy (SEM). X-ray photoelectron spectroscopy (XPS) were conducted to further characterize the electronic and crystal structures. Optical studies reveal that CAIC:Cr^{3+},Yb^{3+} DPSCs show

broadband NIR emission (λ_{max}=1000 nm, FWHM=188 nm) and high PLQY (~45%) with 365 nm excitation. The enhancement mechanism is also discussed. Furthermore, we combined the DPSCs with the 365 nm LED chip to prepare pc-LED and demonstrated applications in vein imaging and night vision.

2. Results and Discussion

The structure of the CAIC:Cr^{3+} DPSCs were determined using SHELXT and OLEX2. The corresponding crystallographic parameters are summarized in Table S1-S4 in SI. The CAIC:Cr^{3+} DPSCs with the traditional perovskite structure with Fm-3m space group where $[AgCl_6]^{5-}$and $[InCl_6]^{3-}$/$[CrCl_6]^{3-}$octahedra share the halide atoms at the corner to form a 3D structure. By introducing Cr^{3+} into the pristine $Cs_2AgInCl_6$ perovskite single crystal structure, lattice parameter and cell volume are reduced from the original magnitude due to the relatively smaller ionic radius of Cr^{3+}, validating that Cr^{3+} ions successfully enter the lattice to partially replace the In^{3+} ions.[27]Figure S1 show SEM images of CAIC, CAIC:30%Cr^{3+} and CAIC:30%Cr^{3+}, 3%Yb^{3+} DPSCs, respectively. As seen from the SEM images, all of them are octahedral shape with average sizes of 500 μm. X-ray diffraction (XRD) of CAIC:Cr^{3+} and CAIC:Cr^{3+},Yb^{3+} DPSCs was also measured, with results shown in Figure 1b. Cubic phase was observed for all the DPSCs samples, with no noticeable impurity detected. The introduction of Cr^{3+} and Yb^{3+} has no effect on the structure of the CAIC. Compared with the XRD results of CAIC:Cr^{3+}, the intensity of the diffraction peaks for the 220 crystal plane increases significantly after introducing Yb^{3+}, indicating greatly improved crystallinity of the DPSCs. Notably, the XRD diffraction peaks for the (220) crystal plane are shifted

monotonically to larger angle with the increase of Cr^{3+} concentration due to substituting smaller Cr^{3+} ions for the larger In^{3+} ions. The XRD patterns of the samples with different amounts of Cr^{3+} and Yb^{3+} are shown in Figures S2 and S3. The diffraction peak of the (220) crystal plane of CAIC:Cr^{3+},Yb^{3+} shifts to a smaller angle compared to that of CAIC:Cr^{3+} due to the larger ion radius of Yb^{3+} than In^{3+} causing lattice expansion.

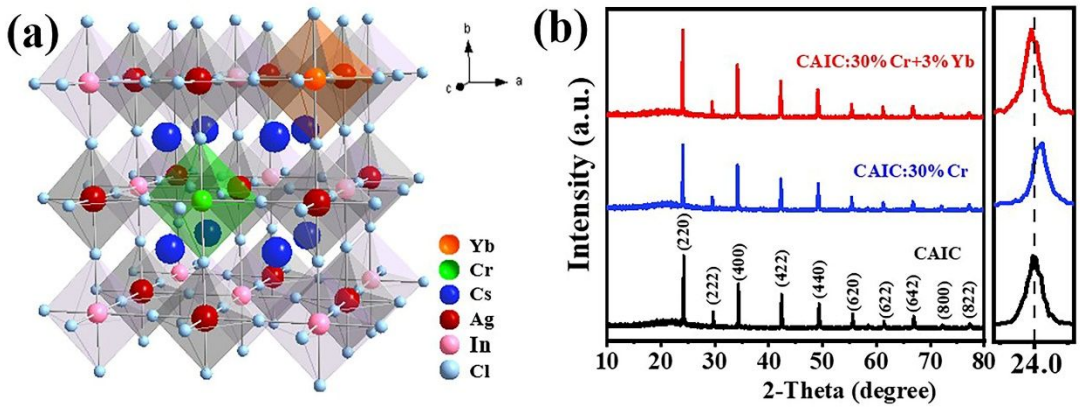

Figure 1. (a) Crystal structure schematic illustration of Cr^{3+}, Yb^{3+} doped CAIC DPSCs. (b) XRD patterns of Cr^{3+}, Yb^{3+} doped CAIC DPSCs and (220) local enlarged view of crystal plane.

EDS spectra were measured to determine the elemental composition of CAIC:30%Cr^{3+}. Figure S4 (a-f) shows EDS images of CAIC:Cr^{3+} DPSCs. Elements of Cs, In, Ag, Cl and Cr are found in the EDS spectrum and evenly distributed in the whole DPSCs. The actual doping content of Cr^{3+} and Yb^{3+} was determined using ICP-OES and ICP-MS, with results given in Table S5, which is lower than the initial content introduced in the synthesis. In the following, we use the feed molar ratio for discussion.

The elemental composition and electronic properties of CAIC:Cr^{3+},Yb^{3+} were

further characterized using XPS, and the results confirm the existence of all the elements in CAIC:Cr^{3+},Yb^{3+} (Figure 2a-f). In the high-resolution Cr 2p spectrum (Figure 2e), the peaks of 587.1 and 576.9 eV can be assigned to Cr $2p_{1/2}$ and Cr $2p_{3/2}$, and no peaks associated with Cr^{4+} are found, supporting that Cr remains in the +3 valence state.[28] A peak at 572.4 eV is assigned to Ag $3p_{3/2}$. The binding energy of Cr 2p is consistent with the binding energy of octahedral Cr^{3+} ions reported in earlier studies.[21, 29] In addition, the peaks of In 3d and Cl 2p all shift toward lower binding energy due to Yb^{3+} incorporation, which is attributed to the smaller electronegativity of Yb than In, leading to stronger Yb-Cl bonding.[30]

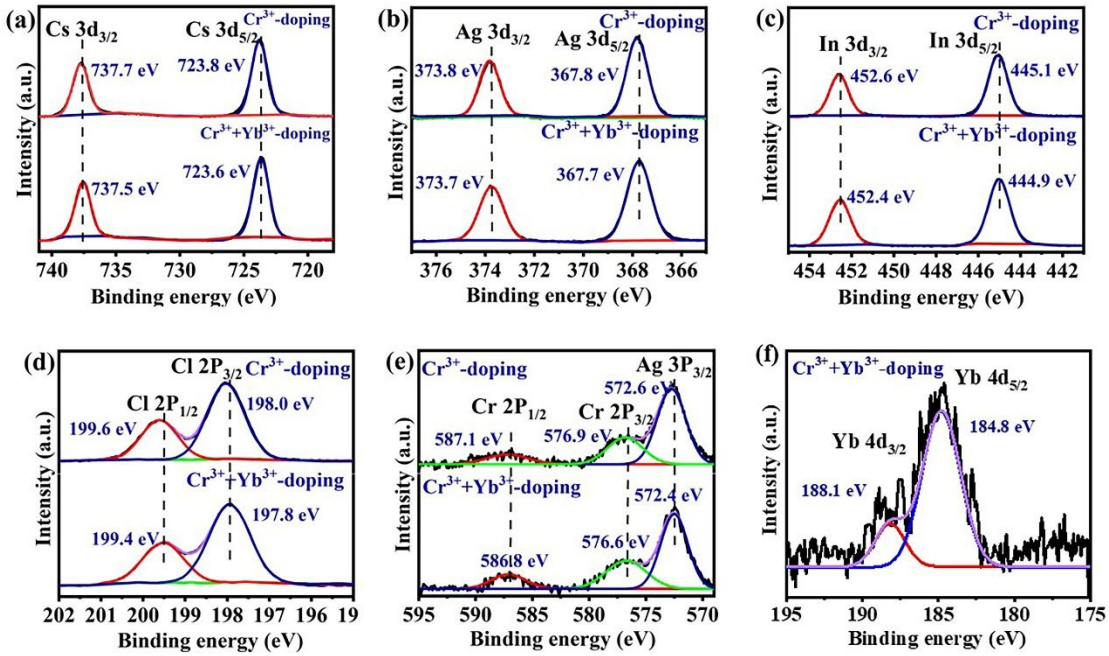

Figure 2. X-ray photoelectron spectroscopy (XPS) core level spectra of (a) Cs 3d, (b) Ag 3d, (c) In 3d, (d) Cl 2p, (e) Cr 2p, (f)Yb 4d.

The diffuse reflectance spectra (DRS) of the samples are shown in Figure 3a. CAIC:Cr^{3+} shows three broad absorption bands with maxima at around 365 nm, 550 nm and 830 nm. The main 365 nm band is attributed to the electronic transition from

the valence to the conduction band of the CAIC host. After calculating and extrapolating using a linear function to the photon energy axis, the bandgap of pristine CAIC is estimated to be about 3.2 eV, as shown in the inset of Figure 3a, which is consistent with a previous report.[31] The absorption bands at 550 nm and 830 nm can be ascribed to Cr^{3+} *d-d* transitions of $^4A_2 \rightarrow {}^4T_1$ and $^4A_2 \rightarrow {}^4T_2$. The DRS spectrum of CAIC:Cr^{3+} and CAIC:Cr^{3+},Yb^{3+} show similar absorption positions. Figure S5 shows PL excitation spectra (PLE) of CAIC:Cr^{3+} and CAIC:Cr^{3+},Yb^{3+} with emission wavelength of 1000 nm monitored. The PLE spectra agree with the DRS spectrum. Besides, the PLE spectra of the Yb-doped sample exhibit identical spectral shapes, indicating that the emission originates from the same transition. The three PLE bands at 365, 550, and 830 nm can be assigned as in the DRS.

PL spectra of CAIC:Cr^{3+},Yb^{3+} DPSCs with 365 nm excitation are shown in Figure 3b. CAIC:30%Cr^{3+} DPSCs have a broadband emission in the range of 800 to1400 nm with maxima at 1000 nm and FWHM=180 nm, which is ascribed to the $^4T_2$-$^4A_2$ transition of Cr^{3+}. The addition of Yb^{3+} does not change the position of the emission band but increases its intensity and FWHM to 188 nm. This broad emission bands covers the NIR-I (700-900 nm) and NIR-II (1000-1700 nm) bio-window, which is broader than many recently reported NIR phosphors, such as $LaMgGa_{11}O_{19}$:Cr^{3+} (138 nm)[32] and $MgTa_2O_6$:Cr^{3+} (140 nm).[33] The increased PL intensity indicates suppressed non-radiative recombination by Yb^{3+} doped CAIC:Cr^{3+}. The PLQY of the best sample is about 45% (Figure S6) which is much higher than $Cs_2NaInCl_6$:Cr^{3+} (PLQY=19.7%) and $Cs_2AgInCl_6$:Yb^{3+} (PLQY=0.2%).[16,34] The PL spectra of Yb-doping CAIC:Cr^{3+} with

different Yb^{3+} concentrations, as shown in Figure S7, exhibit a blue-shift for CAIC:Cr^{3+},Yb^{3+} DPSCs compared with the CAIC:Cr^{3+} DPSCs, which is attributed to passivation of shallow trap states in CAIC:Cr^{3+},Yb^{3+} DPSCs as discussed in more details later.[35,36]

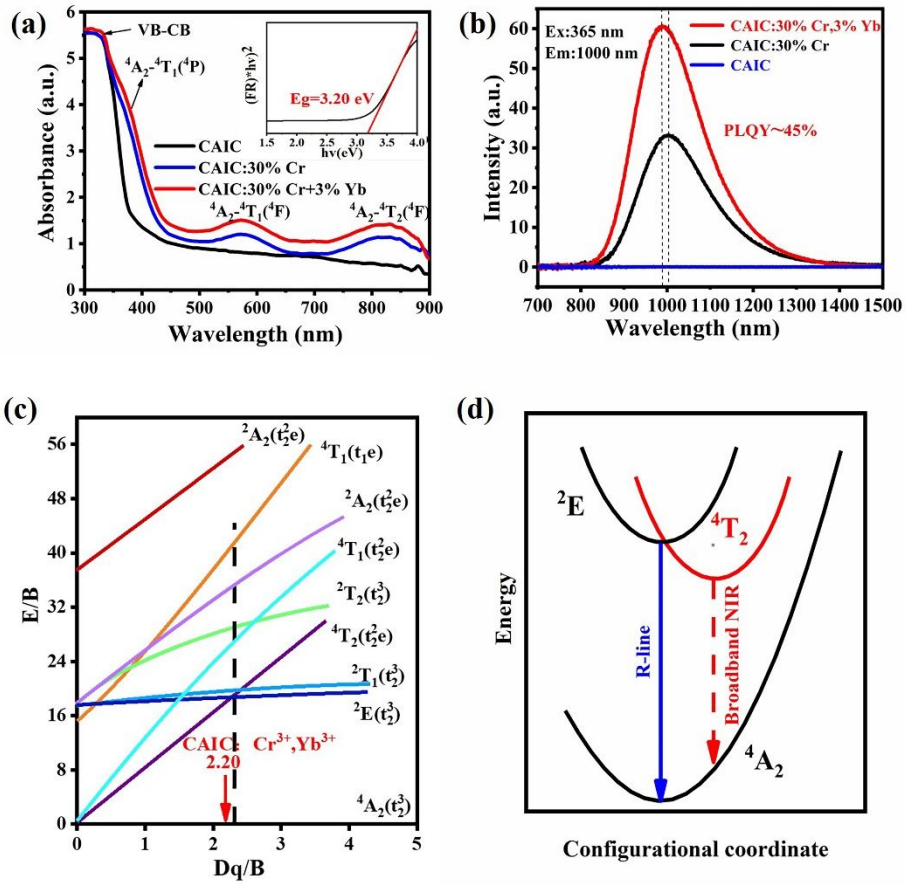

Figure 3. (a) DRS of CAIC:Cr^{3+},Yb^{3+}. The inset shows the DR spectrum of the CAIC DPSCs host with $[F(R)*hv]^2$ as a function of photon energy, for determining the band gap energy. (b) PL spectra of CAIC:Cr^{3+},Yb^{3+} DPSCs. (c) Tanabe-Sugano energy level diagram of Cr^{3+} in an octahedral crystal field. (d) Configurational coordinate diagram of Cr^{3+} in a week crystal field.

The PL spectra with different excitation wavelengths shown in Figure S8 vary in intensity but maintain the same shape with excitation wavelength changing from 320 to 600 nm, indicating that the NIR emission originates from the same transition. In addition, we used the same method to synthesize CAIC:Yb^{3+}, with its PL spectrum shown in Figure S9. The emission band of CAIC:Yb^{3+} has the same position as that of CAIC:Cr^{3+}, but have the different emission origin. The emission of CAIC:Cr^{3+} can be ascribed to Cr^{3+} *d-d* transitions and emission of CAIC:Yb^{3+} can be attributed to $^2F_{5/2}\rightarrow{}^2F_{7/2}$ transition of Yb^{3+} *f* electrons and thus exhibits a narrower FWHM and lower PLQY. [16]

Upon introducing Cr^{3+} to $Cs_2AgInCl_6$, Cr^{3+} ions (r =0.62 Å, CN=6) are proposed to substitute In^{3+} ions (r=0.8 Å, CN=6) due to their similar ionic radius and same oxidation state, forming $[CrCl_6]^{3-}$ octahedron.[37,38] Because the symmetry decrease of the potential octahedron field, the 3d orbital of Cr^{3+} ion degrades to the double degenerated d_{x2-y2} and d_{z2} (e_g) states and the triple degenerated d_{xy}, d_{xz}, and d_{yz} (t_{2g}) states. This process can be explained by the Tanabe-Sagano diagram (Figure 3c).[39] The emission of Cr^{3+} ions are strongly depend on the crystal field environment of the lattice. In the case of a strong crystal field, the transition from the ^2E to the $^4A_2$ energy level is spin-forbidden, resulting in narrowband red light from ^2E energy level (marked as R-line in Figure 3d). In a weak crystal field, the $^4T_2$ energy level transitions to the ground state are allowed, resulting broadband NIR light from the $^4T_2$ energy level. According to energy level splitting, the crystal field strength is defined by relative positions of the $^4T_2$ and ^2E energy levels.[40] The following equations can be used to obtain *Dq/B*:

$$Dq=E(^4A_2\rightarrow{}^4T_2)/10 \quad (1)$$

$$\frac{Dq}{B}=\frac{15(\frac{\Delta E}{Dq}-8)}{(\Delta E/Dq)^2-10(\Delta E/Dq)} \quad (2)$$

where E($^4A_2\rightarrow{}^4T_2$) is the energy difference between $^4T_2$ and $^4A_2$ energy levels (in cm^{-1}), ΔE is the energy difference between E ($^4A_2\rightarrow{}^4T_1$) and E ($^4A_2\rightarrow{}^4T_2$) transitions. *Dq* is called the crystal field splitting parameter, and *B* is Racah parameters. Using the data in Figure 3a, the values of *Dq*/*B* are 2.20 and 2.25 (Figure 3c) in CAIC:Cr^{3+},Yb^{3+} DPSCs and in CAIC:Cr^{3+}, respectively. When the *Dq/B* value is larger than 2.3, Cr^{3+} ions are in a strong crystal field. When the *Dq/B* value is smaller than 2.3, Cr^{3+} ions are in a weak crystal field.[41] This indicates that the Cr^{3+} ions are in a weak crystal field in the CAIC:Cr^{3+},Yb^{3+} host. As shown in Figure 3c, the energy separation between energy levels $^4T_2$ and $^4A_2$ is narrow. Therefore, the CAIC:Cr^{3+},Yb^{3+} exhibits broadband NIR emission (800 to 1400 nm), and the emission band is centered at much longer wavelength (1000 nm) than other Cr^{3+}-doped NIR phosphors such as $BaMgAl_{10}O_{17}$:Cr^{3+} (762 nm)[42] and $LiScP_2O_7$:0.06Cr^{3+}(880 nm).[43]

To gain deeper insight into the PL mechanism of the Yb^{3+}-doped CAIC:Cr^{3+} DPSCs, we measured the time-resolved PL (TRPL) decay profiles, as shown in Figure 4a. The TRPL of CAIC:Cr^{3+},Yb^{3+} was collected with excitation at 365 nm and emission monitored at 1000 nm. All of the decay curves are fit by a single exponential function, with time constant on the microsecond time scale, which is consistent with previous report.[22] This also indicates that the emission is mainly from the transition of $^4T_2$ to $^4A_2$ of Cr^{3+}. We can use equation (3) and (4) to calculate radiative (τ_r) and non-radiative

(τ_{nr}) components of the observed PL lifetime (τ_{obs}).

$$PLQY = \frac{\tau_{0bs}}{\tau_r} \quad (3)$$

$$\frac{1}{\tau_{0bs}} = \frac{1}{\tau_r} + \frac{1}{\tau_{nr}} \quad (4)$$

Calculated values for τ_r and τ_{nr} are summarized in Table 1. Both radiative and non-radiative lifetimes increase significantly with Yb^{3+} doping. This indicates that Yb^{3+} doping affects both the radiative and non-radiative pathways. The effect on radiative pathways suggests electronic interaction between Cr^{3+} and Yb^{3+} ions. The longer non-radiative lifetime may be attributed to lower density of trap states upon Yb^{3+} co-doping that has some passivation effect on defects.[44]

Table 1 Calculated Radiative and Nonradiative Lifetimes for CAIC:30%Cr^{3+} and CAIC:30%Cr^{3+},3%Yb^{3+}.

sample	τ_{obs} (μs)	τ_r (μs)	τ_{nr} (μs)	PLQY
CAIC:30%Cr^{3+}	10.81	48.0	14.0	22.5%
CAIC:30%Cr^{3+},3%Yb^{3+}	32.03	71.1	58.5	45%

Ln^{3+} doping has been suggested to passivate anion defects due to strong Ln-X bonding that reduces the formation of defects and lengthen exciton lifetime of perovskites.[36,45] The PL spectra and TRPL profiles of CAIC:Cr^{3+},Er^{3+} and CAIC:Cr^{3+},Ho^{3+} DPSCs were measured and shown in Figure S10 and Figure S11. Doping Ho^{3+} or Er^{3+} to CAIC:Cr^{3+} DPSCs also leads to enhanced PL intensity and longer observed PL lifetime (15.30 μs and 20.48 μs). Compared to Ho^{3+} and Er^{3+}, Yb^{3+} with relatively smaller electronegativity and ionic radius has a stronger effect on the PL properties. The smaller electronegativity and ionic radius Yb^{3+} is expected to lead to stronger Yb-Cl bonding,[30]

which is supported by XPS results. The strong interaction between Yb^{3+} and Cl^{-} can improve crystallinity, reduces the surface energy of crystal growth, Cl^{-} anions will firstly interact with Yb^{3+} which rendering Yb^{3+} absorbed on the colloidal cluster to form large grains to improves the crystallinity and reduce the formation of defects.[23,46] The origin for PL enhancement in CAIC:Cr^{3+},Yb^{3+} DPSCs is attributed to structural modification upon Yb^{3+} doping, as illustrated in Figure 4b. The pristine perovskite structure possesses more Cl vacancies (V_{Cl}) and In_{Ag} vacancies (represented by black sphere).[47] The ionic radius of Yb^{3+} ion is closer to that of In^{3+} ion than Cr^{3+}, thus the addition of Yb^{3+} ion alleviates the distorted $[InCl_6]^{3-}$ octahedra caused by the addition of Cr^{3+} ion and the introduction of Yb^{3+} can reduces the surface energy to influence the growth of crystals. As a result, the PL intensity of the NIR-II emission is enhanced by doping with Yb^{3+}.

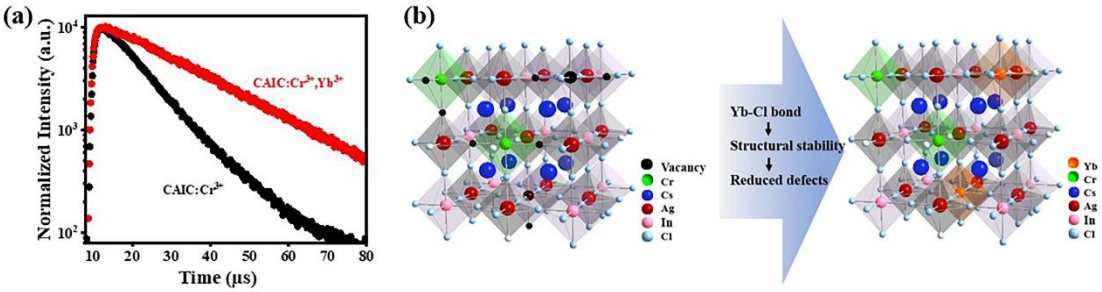

Figure 4. (a) Time-resolved PL decay profiles of CAIC:Cr^{3+}, and CAIC:Cr^{3+},Yb^{3+}. (b) Schematic illustration of the structure of CAIC:Cr^{3+} DPSCs with defects and CAIC:Cr^{3+},Yb^{3+} with structural modification.

To determine the role of Yb^{3+} incorporation in boosting the Cr^{3+} emission, we measured the PL spectra of CAIC, CAIC:Cr^{3+}, CAIC:Yb^{3+}, CAIC:Cr^{3+},Yb^{3+} samples in the 450-800 nm region, as shown in Figure S12a, in which the host emission intensity

is improved with Yb^{3+} doping. Figure S12b shows the spectral overlap between the PLE band of CAIC:Cr^{3+} monitored at 1000 nm and the PL spectrum of CAIC:Yb^{3+}excited at 365 nm. We suggest that there is energy transfer (ET) from the STEs to Cr^{3+} in the co-doped CAIC. Moreover, the incorporation of the Yb^{3+} ions can induce an elongation of the bond lengths of the $[CrCl_6]^{3-}$ octahedra associated with and thus, a decrease of the energy gap between the $^2E(g)$ and $^4T_2(g)$ states of Cr^{3+}, which triggers the occurrence of structural confinement effect and promoting the ET of STEs to Cr^{3+}.[48,49] Overall, as shown in Figure S13, we attribute the enhancement of PL to the synergistic effect of reduced non-radiative recombination due to defect passivation and energy transfer from STEs to Cr^{3+}.

To further understand the effect of Yb^{3+} ion doping on thermal stability of the samples, the PL spectra of CAIC:Cr^{3+} and CAIC:Cr^{3+},Yb^{3+} DPSCs at different temperatures were measured, as shown in Figure 5a-b. Figure S13 illustrates the photophysical process in Cr^{3+}-incorporated CAIC DPSCs. With photoexcitation at 365 nm, the electrons are excited from the valence band (VB) to the conduction band (CB) of the CAIC DPSCs host. The energy from the host can be transferred to the $^4T_2$ state of Cr^{3+} ions that then results in the $^4T_2$–$^4A_2$ transition. The energy of the host can also be transferred to the self-trapped exciton (STE) state, resulting in a broad emission (Process 1),[54] or to Cr^{3+} ion (Process 2) that leads to the $^4T_2$–$^4A_2$ transition. Figure S14 shows the PL spectra in the visible region of the CAIC:30%Cr^{3+} sample at 80 K and 200 K, which originates from process 1 in Figure S13. The emission of STEs is

observed at low temperature and quenched at above 200 K. From 80K to 200K, the PL in the visible region decreases with the increasing temperature due to electron-phonon coupling thermal, at the same time, the NIR emission increases due to much energy transfer from the STEs to Cr^{3+}, which is similar to previous reports.[50-53] With further increase in temperature, the emission decreased, attributed to the increase of non-radiative transition processes mediated by phonons. At 350 K, CAIC:Cr^{3+} and CAIC:Cr^{3+},Yb^{3+} DPSCs keep 15.47% and 49.61% of their original intensities at 80 K, indicating that the thermal stability of the material was improved with the addition of Yb^{3+} (Figure 5c). This may be related to the difference in electron-phonon coupling between CAIC:Cr^{3+} and CAIC:Cr^{3+},Yb^{3+}. Generally, we can use equation (5) to calculate coupling effect between electrons and phonons by fitting FWHM of the PL spectrum with temperatures.[55]

$$FWHM = 2.36\sqrt{S}\hbar\omega\sqrt{coth\left(\frac{\hbar\omega}{2kT}\right)} \quad (5)$$

where $\hbar\omega$ stands for the phonon frequency, T is the Kelvin temperature, S means the Huang-Rhys parameter and k means the Boltzmann constant. When regrading $\frac{\hbar\omega}{2kT}$ as x, coth(x) is equivalent to $\frac{e^x + e^{-x}}{e^x - e^{-x}}$. Owing to $\frac{\hbar\omega}{2kT} = 10^{-3}$, equation (5) can be simplified as equation (6).

$$FWHM^2 = 5.57 \times S \times (\hbar\omega)^2\left(1 + \frac{1}{\frac{\hbar\omega}{2kT}}\right) \quad (6)$$

Equation (6) can be written as :

$$FWHM^2 = A \times 2kT + B \quad (7)$$

where A = 5.57× S× $\hbar\omega$, B = 5.57× S× $(\hbar\omega)^2$. The fitting results are depicted in Figure 5d. The $\hbar\omega$ and S for CAIC:Cr^{3+} are 0.0305 eV and 3.16, and those for

CAIC:Cr^{3+},Yb^{3+} are 0.0296 eV and 3.01, revealing strong electron-phonon coupling effect in CAIC:30%Cr^{3+}. A smaller *S* value suggests the electron-phonon coupling effect in CAIC:Cr^{3+},Yb^{3+} is weaker than CAIC:Cr^{3+}. Therefore, the thermal stability of CAIC:Cr^{3+},Yb^{3+} is stronger than that of CAIC:Cr^{3+}. Furthermore, we calculated exciton binding energy of CAIC:30%Cr^{3+} and CAIC:30%Cr^{3+},3%Yb^{3+} using temperature-dependent PL spectra (Figure 5a and 5b), from which the corresponding exciton binding energy (E_b) is derived as 215 meV and 242 meV (Figure S15) according to Equation 8.

$$I(\mathrm{T}) = \frac{I_0}{1 + Ae^{\left(-\frac{E_b}{kT}\right)}} \quad (8)$$

Combined with the calculated optical phonon energy analysis, we suggest that the CAIC:30%Cr^{3+},3%Yb^{3+} DPSCs samples have higher exciton binding energy and relatively lower phonon disturbance, indicating suppressed non-radiative relaxation.[42,56] Therefore, doping Yb^{3+} could effectively suppress the strong exciton–phonon interaction and improve radiative transition probability and PLQY. This facilitates the application of crystals for near-infrared light emission and light-emitting device. In addition, the NIR emission band center position shifts from 964 to 1000 nm as the temperature increases from 80 to 380 K, which can be explained by the change in crystal field strength. As the temperature rises, the lattice vibration increases and the lattice expands, which ultimately weakens the crystal field. According to the Tanabe-Sugano energy level diagram of Cr^{3+} (Figure 3c), a weakening of the crystal field will result in a red-shift of the emission spectrum.[57]

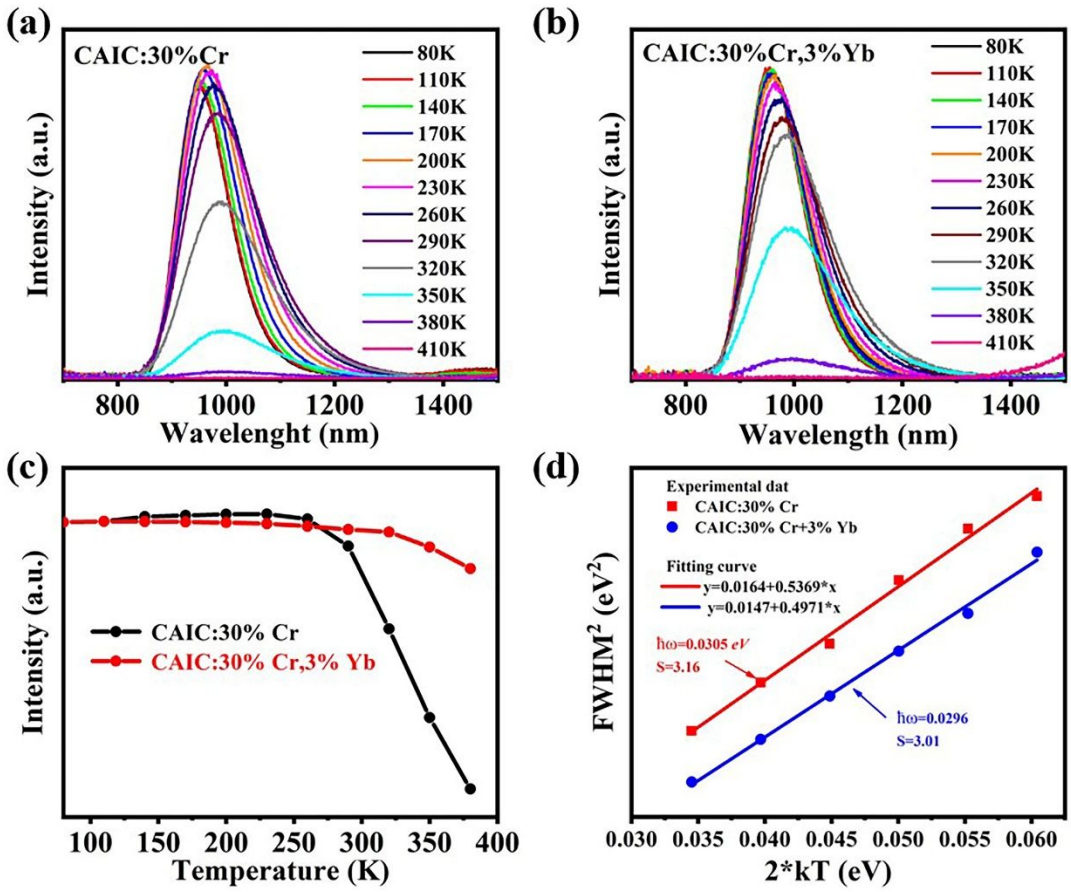

Figure 5. Temperature-dependent PL spectra of (a) CAIC:Cr^{3+} excited at 365 nm and (b) CAIC:Cr^{3+}, Yb^{3+}excited at 365 nm. (c) The dependence of the PL intensity of CAIC:Cr^{3+} and CAIC:Cr^{3+},Yb^{3+} on temperature. (d) The fitting results of $FWHM^2$ as a function of 2kT.

As a demonstration of potential applications, the CAIC:Cr^{3+},Yb^{3+} DPSCs were applied with InGaN chip (λ_{em}=365 nm) to prepare NIR pc-LED samples. Figure 6a shows the driving current dependent electroluminescence (EL) spectra of the pc-LED device. The NIR EL intensity increases with increasing current. Besides, Figure 6b shows the NIR output of 18.0 mW@190 mA, and conversion efficiency reaches 9.45% @10mA. We used the prepared pc-LED to test muscle tissue transmission, human vein imaging, and night vision ability, as shown in Figure 6c. The results show that intensity

of NIR radiation is sufficient to penetrate a 2.5 cm chicken breast (Figure 6ci), and the vein distribution of the palm can be clearly observed (Figure 6cii). In addition, a photon of an orange is taken with a visible light camera under light (Figure 6ciii) and in the dark (Figure 6civ). When the NIR-LED is turned on, the orange can be seen by the NIR camera (Figure 6cv). These results suggest that the CAIC:Cr^{3+},Yb^{3+} is promising for human vein imaging and night vision.

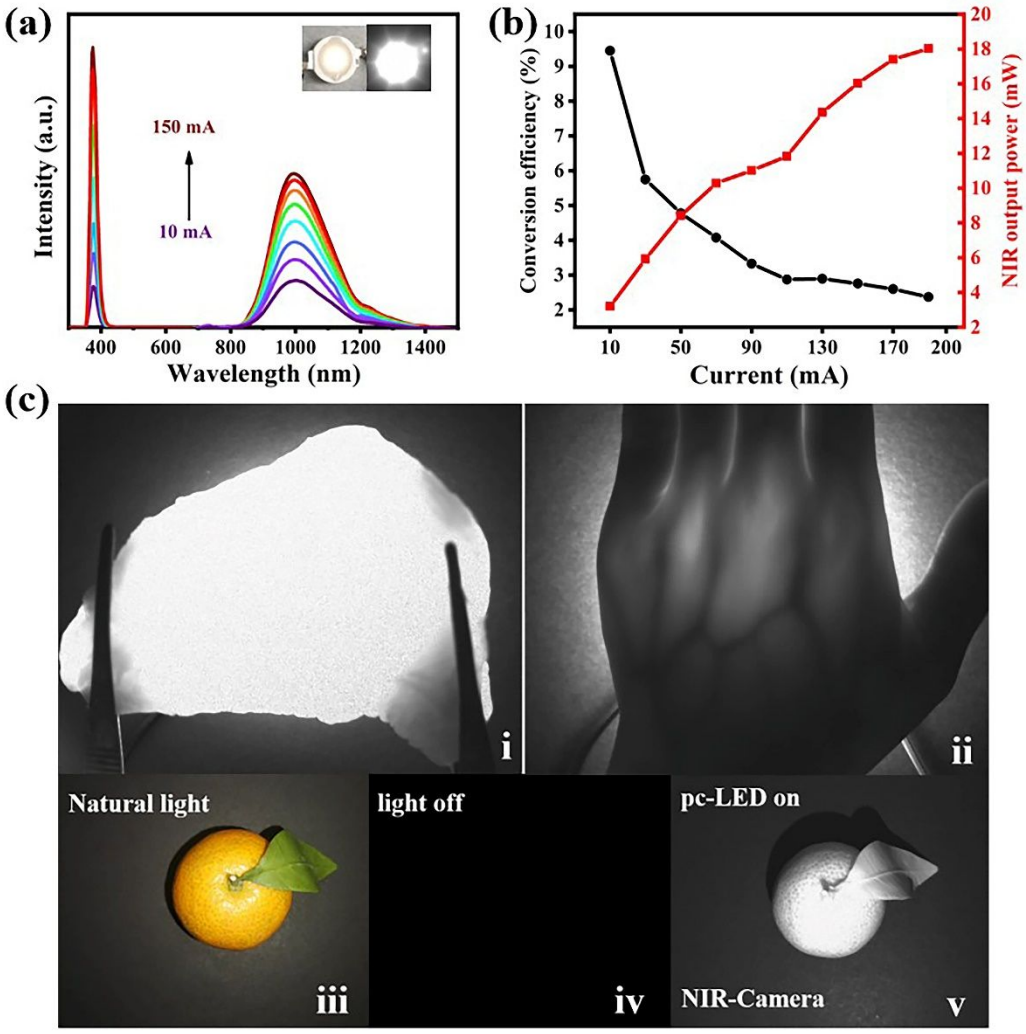

Figure 6. (a) Driven current dependent emission spectra of fabricated NIR pc-LED. (b) conversion photoelectric efficiency and NIR output power of pc-LED. (c) Photograph of the transmission photographs of a 2.5 cm chicken breast (i) and the veins

in the palm (ii) taken with a NIR camera. (iii-v) A photo of an orange taken with natural light on (iii) and off (iv) captured with a visible camera and NIR pc-LED light by an NIR camera (v).

3. Conclusion

In conclusion, we synthesized a broadband NIR co-doped CAIC:Cr^{3+},Yb^{3+} DPSCs by a facile hydrothermal method. Under 365 nm excitation, the as-prepared co-doped CAIC:Cr^{3+},Yb^{3+} DPSCs shows a broadband NIR emission at 1000 nm with the full-width at half maximum (FWHM) of 188 nm and PLQY ~45%. The enhanced PLQY is attributed to is attributed to the synergistic effect of reduced non-radiative recombination due to defect passivation and increase in crystallinity, and energy transfer (ET) of STEs to Cr^{3+}. With the aid of a NIR camera, pc-LED was fabricated and used as a light source to capture clear images of veins in the palm. Furthermore, the feasibility of pc-LED for night vision applications was successfully demonstrated. This study suggests that the synthesized CAIC:Cr^{3+},Yb^{3+} DPSCs are promising for biomedical imaging applications.

Acknowledgement

This work was supported by the National Natural Science Foundation of China (Grant No. 21965003) and the Opening Project of Guangxi Key Laboratory of Marine Natural Products and Combinatorial Biosynthesis Chemistry (Grant No. GXMNPC2020003, JZZ acknowledges the US NSF (CHE-1904547) for financial support.

ASSOCIATED CONTENT

Supporting Information

Experimental sections; XRD patterns of CAIC: x%Cr(x = 0, 10, 20, 30, 40, 50) DPSCs; XRD patterns of CAIC:30%Cr, y%Yb (y = 0, 1, 2, 3) DPSCs; SEM image and EDS spectra of CAIC:30%Cr with the corresponding atomic maps; PLE spectra of CAIC:30%Cr^{3+},y%Yb^{3+} (y= 0, 1, 2, 3); PL spectra of CAIC:30%Cr^{3+},y%Yb^{3+} (y = 0, 1, 2, 3). The incorporated samples were tested at λ_{ex}= 365 nm; Excitation-wavelength-dependent (320-600 nm) PL spectra of CAIC:30%Cr^{3+},3%Yb^{3+}; PL spectra of CAIC:30%Cr^{3+},3%Yb^{3+} and CAIC:Yb^{3+}. The emission spectrum of CAIC:Yb^{3+} in the figure is magnified tenfold; PL curves measured from CAIC:Cr^{3+} and CAIC:Ln^{3+} samples; TRPL decay curves of CAIC:Cr^{3+} doped with or without Ln^{3+} ions; Details of X-ray crystallographic parameters of single crystals; Details of atoms occupation situation of $Cs_2AgIn_{0.7}Cr_{0.3}Cl_6$ single crystal; Cr^{3+} and Yb^{3+} content from starting materials and measured by ICP.

Notes

The authors declare no competing financial interest

References

(1) M. Mao, T. Zhou, H. Zeng, L. Wang, F. Huang, X. Tang and R.-J. Xie, Broadband Near-infrared (NIR) Emission Realized by the Crystal-field Engineering of $Y_{3-x}Ca_xAl_{5-x}SixO_{12}:Cr^{3+}$(x= 0-2.0) Garnet Phosphors, *J. Mater. Chem. C.,* 2020**, 8**,

1981-1988.

(2) D. Dai, Z. Wang, Z. Xing, X. Li, C. Liu, L. Zhang, Z. Yang and P. Li, Broad Band Emission Near-infrared Material $Mg_3Ga_2GeO_8:Cr^{3+}$: Substitution of Ga-In, Structural Modification, Luminescence Property and Application for High Efficiency LED. *J. Alloy. Compd.,* 2019**, 806**, 926-938.

(3) T. Appadurai, S. Chaure, M. Mala and A. K. Chandiran, Role of Copper in Enhancing Visible Light Absorption in $Cs_2Ag(Bi, In, Sb)Cl_6$ Halide Double-Perovskite Materials. *Energ. Fuel.,* 2021, **35**, 11479-11487.

(4) R. Marin and D. Jaque, Doping Lanthanide Ions in Colloidal Semiconductor Nanocrystals for Brighter Photoluminescence. *Chem Rev*., 2021, **121**, 1425-1462.

(5) I. Infante and L. Manna, Are There Good Alternatives to Lead Halide Perovskite Nanocrystals. *Nano Lett.,* 2021, **21**, 6-9.

(6) H. Arfin, A. S. Kshirsagar, J. Kaur, B. Mondal, Z. Xia, S. Chakraborty and A. Nag, ns^2 Electron (Bi^{3+} and Sb^{3+}) Doping in Lead-Free Metal Halide Perovskite Derivatives. *Chem. Mater.,* 2020, **32**, 10255-10267.

(7) F. Igbari, Z. -K. Wang and L. -S. Liao, Progress of Lead-Free Halide Double Perovskites. *Adv. Energy Mater.,* 2019, **9**, 1803150.

(8) K. Dave, M. H. Fang, Z. Bao, H. T. Fu and R. S. Liu, Recent Developments in Lead-Free Double Perovskites: Structure, Doping, and Applications. *Chem Asian J.,* 2020, **15**, 242-252.

(9) R. Sun, D. Zhou and H. Song, Rare Earth Doping in Perovskite Luminescent Nanocrystals and Photoelectric Devices. *Nano Select.,* 2021, **3**, 531-554.

(10) J. Zhou, X. Yun, R. Wang, D. Xu and X. Li, Self-trapped Exciton to Dopant Energy Transfer in Sb^{3+}-doped Cs_2ZrCl_6 Perovskite Variants. *Mater. Chem. Front.,* 2021, **5**, 6133.

(11) Y. Yao, S.-W. Zhang, Z. Liu, C.-Y. Wang, P. Liu, L. Ma, G. Wei and F. Kang, Air Stable and Highly Efficient Bi^{3+}-doped Cs_2SnCl_6 for Blue Light-emitting Diodes. *RSC Adv.,* 2021, **11**, 26415-26420.

(12) Z. Xu, W. Liu, Z. Wang and L. Hanzo, Petahertz Communication: Harmonizing Optical Spectra for Wireless Communications. *Digit. Commun. Netw.,* 2021, **7**, 605-614.

(13) Y. Tang, S. Tang, M. Luo, Y. Guo, Y. Zheng, Y. Lou and Y. Zhao, All-inorganic Lead-Free Metal Halide Perovskite Quantum Dots: Progress and Prospects. *Chem. Commun.,* 2021, **57**, 7465-7479.

(14) J. Zhou, X. Rong, M.S. Molokeev, Y. Wang, X. Yun, D. Xu and X. Li, Alloying Cs^+ into Rb_2ZrCl_6:Te^{4+} Toward Highly Efficient and Stable Perovskite Variants. *Mater. Chem. Front.,* 2021, **5**, 4997-5003.

(15) Y. Liu, A. Nag, L. Manna and Z. Xia, Lead-Free Double Perovskite $Cs_2AgInCl_6$. *Angew. Chem. Int. Ed.,* 2021, **60**, 11592-11603.

(16) Y. Mahor, W.J. Mir and A. Nag, Synthesis and Near-Infrared Emission of Yb-Doped $Cs_2AgInCl_6$ Double Perovskite Microcrystals and Nanocrystals. *J. Phys. Chem. C.,* 2019, **123**, 15787-15793.

(17) H. Arfin, J. Kaur, T. Sheikh, S. Chakraborty and A. Nag, $Bi(^{3+})$ -$Er(^{3+})$ and $Bi(^{3+})$ -$Yb(^{3+})$ Codoped $Cs_2AgInCl_6$ Double Perovskite Near-Infrared Emitters. *Angew. Chem.*

Int. Ed., 2020, **59**, 11307-11311.

(18) Q. Zhang, G. Li, P. Dang, D. Liu, D. Huang, H. Lian and J. Lin, Enhancing and Tuning Broadband Near-infrared (NIR) Photoluminescence Properties in Cr^{3+}-doped $Ca_2YHf_2Al_3O_{12}$ Garnet Phosphors via Ce^{3+}/Yb^{3+}-codoping for LED Applications. *J. Mater. Chem. C.,* 2021, **9**, 4815-4824.

(19) D. Hou, H. Lin, Y. Zhang, J.-Y. Li, H. Li, J. Dong, Z. Lin and R. Huang, A broadband near-infrared phosphor $BaZrGe_3O_9:Cr^{3+}$: luminescence and application for light-emitting diodes, *Inorg. Chem. Front.*, 2021, **8**, 2333-2340.

(20) Z. Wu, X. Han, Y. Zhou, K. Xing, S. Cao, L. Chen, R. Zeng, J. Zhao and B. Zou, Efficient Broadband Near-infrared Luminescence of Cr^{3+} Doped Fluoride K_2NaInF_6 and Its NIR-LED Application toward Veins Imaging. *Chem. Eng. J.,* 2022, **427**, 131740.

(21) W. Zhou, J. Luo, J. Fan, H. Pan, S. Zeng, L. Zhou, Q. Pang and X. Zhang, Luminescent Properties and LED Application of Broadband Near-Infrared Emitting $NaInGe_2O_6:Cr^{3+}$ phosphors. *Ceram. Int.,* 2021, **47**, 25343-25349.

(22) F. Zhao, Z. Song, J. Zhao and Q. Liu, Double perovskite $Cs_2AgInCl_6:Cr^{3+}$: broadband and near-infrared luminescent materials. *Inorg. Chem. Front.,* 2019, **6**, 3621-3628.

(23) K. Wang, L. Zheng, T. Zhu, X. Yao, C. Yi, X. Zhang, Y. Cao, L. Liu, W. Hu and X. Gong, Efficient Perovskite Solar Cells by Hybrid Perovskites Incorporated with Heterovalent Neodymium Cations. *Nano Energy,* 2019, **61**, 352-360.

(24) J. S. Yao, J. Ge, B. N. Han, K. H. Wang, H. B. Yao, H. L. Yu, J. H. Li, B. S. Zhu, J. Z. Song, C. Chen, Q. Zhang, H. B. Zeng, Y. Luo and S. H. Yu, Ce^{3+}-Doping to

Modulate Photoluminescence Kinetics for Efficient $CsPbBr_3$ Nanocrystals Based Light-Emitting Diodes. *J. Am. Chem. Soc.,* 2018, **140**, 3626-3634.

(25) L. Wang, H. Zhou, J. Hu, B. Huang, M. Sun, B. Dong, G. Zheng, Y. Huang, Y. Chen, L. Li, Z. Xu, N. Li, Z. Liu, Q. Chen, L. -D, Sun and C. -H. Yan, A Eu^{3+}-Eu^{2+} Ion Redox Shuttle Imparts Operational Durability to Pb-I Perovskite Solar Cells. *Science,* 2019, **363**, 265–270.

(26) D. Huang, Q. Ouyang, H. Xiao, B. Wang, H. Lian, Q. Zeng and J. Lin, Cr,Yb-codoped $Ca_2LaHf_2Al_3O_{12}$ Garnet Phosphor: Electronic Structure, Broadband NIR Emission and Energy Transfer Properties, *Dalton Trans.*, 2021, **50**, 908-916.

(27) H. Yin, Y. Xian, Y. Zhang, W. Chen, X. Wen, N. U. Rahman, Y. Long, B. Jia, J. Fan and W. Li, An Emerging Lead-Free Double-Perovskite $Cs_2AgFeCl_6$:In Single Crystal, *Adv. Funct. Mater.*, 2020, **30**, 2002225.

(28) X. Duan, J. Liu, Y. Wu, F. Yu and X. Wang, Structure and Luminescent Properties of Co^{2+}/Cr^{3+} Co-doped $ZnGa_2O_4$ Nanoparticles. *J. Lumin.,* 2014, **153**, 361-368.

(29) A. M. Salvi, J. E. Castle, J. F. Watts and E. Desimoni, Peak Fitting of the Chromium 2p XPS Spectrum. *Appl. Surf. Sci.,* 1995, **90**, 333-341.

(30) C. Lu, J. Zhang, D. Hou, X. Gan, H. Sun, Z. Zeng, R. Chen, H. Tian, Q. Xiong, Y. Zhang, Y. Li and Y. Zhu Calcium Doped $MAPbI_3$ with Better Energy State Alignment in Perovskite Solar Cells. *Appl. Phys. Lett.,* 2018, **112**, 193901.

(31) J. Zhou, Z. Xia, M. S. Molokeev, X. Zhang, D. Peng and Q. Liu, Composition Design, Optical Gap and Stability Investigations of Lead-free Halide Double Perovskite $Cs_2AgInCl_6$. *J. Mater. Chem. A.,* 2017, **5**, 15031-15037.

(32) S. Liu, Z. Wang, H. Cai, Z. Song and Q. J. I. C. F. Liu, Highly Efficient Near-infrared Phosphor $LaMgGa_{11}O_{19}:Cr^{3+}$. *Inorg. Chem. Front.,* 2020, **7**, 1467-1473.

(33) G. Liu, M. S. Molokeev, B. Lei and Z. J. J. o. M. C. C. Xia, Two-site Cr^{3+} Occupation in the $MgTa_2O_6:Cr^{3+}$ Phosphor toward Broad-band Near-infrared Emission for Vessel Visualization. *J. Mater. Chem. C.,* 2020, **8**, 9322-9328.

(34) A. Zhang, Y. Liu, G. Liu and Z. Xia, Dopant and Compositional Modulation Triggered Broadband and Tunable Near-Infrared Emission in $Cs_2Ag_{1-x}Na_xInCl_6:Cr^{3+}$ Nanocrystals. *Chem. Mater.,*2022, **34**, 3006–3012.

(35) J. Zhuang, P. Mao, Y. Luan, X. Yi, Z. Tu, Y. Zhang, Y. Yi, Y. Wei, N. Chen, T. Lin, F. Wang, C. Li and J. Wang, Interfacial Passivation for Perovskite Solar Cells: The Effects of the Functional Group in Phenethylammonium Iodide. *ACS Energy Lett.,* 2019, **4**, 2913-2921.

(36) X. Zhuang, R. Sun, D. Zhou, S. Liu, Y. Wu, Z. Shi, Y. Zhang, B. Liu, C. Chen, D. Liu and H. Song, Synergistic Effects of Multifunctional Lanthanides Doped $CsPbBrCl_2$ Quantum Dots for Efficient and Stable $MAPbI_3$ Perovskite Solar Cells. *Adv. Funct. Mater.,* 2022, **18**, 2110346.

(37) P. R. Varadwaj, $A_2AgCrCl_6$ (A = Li, Na, K, Rb, Cs) halide double perovskites: a transition metal-based semiconducting material series with appreciable optical characteristics, *Phys. Chem. Chem. Phys*., 2020, **22**, 24337-24350.

(38) Z. Zou, X. Tang, C. Wu, D. Wang, J. Zhang, Z. Ci, S. Du and Y. Wang, How to tune trap properties of persistent phosphor: Photostimulated persistent luminescence of $NaLuGeO_4:Bi^{3+},Cr^{3+}$ tailored by trap engineering, *Mater. Res. Bull.*, 2018, **97**, 251-259.

(39) H. Xia, J. Wang, H. Wang, J. Zhang, Y. Zhang and T. Xu, Optical Spectroscopy and Crystal-field Strength of Cr^{3+} in Various Solid Matrixes. *Rare Metals,* 2006, **25**, 51-57.

(40) A. Lever, The Crystal Field Splitting Parameter Dq: Calculation and Significance. *Werner Centennial*, 1967.

(41) H. Zeng, T. Zhou, L. Wang and R.-J. Xie, Two-Site Occupation for Exploring Ultra-Broadband Near-Infrared Phosphor-Double-Perovskite $La_2MgZrO_6:Cr^{3+}$. *Chem. Mater.,* 2019, **31**, 5245-5253.

(42) L. You, R. Tian, T. Zhou and R.-J. Xie, Broadband Near-infrared Phosphor $BaMgAl_{10}O_{17}:Cr^{3+}$ Realized by Crystallographic Site Engineering. *Chem. Eng. J.,* 2021, **417**, 129224.

(43) L. Yao, Q. Shao, S. Han, C. Liang, J. He and J. Jiang, Enhancing Near-Infrared Photoluminescence Intensity and Spectral Properties in Yb^{3+} Codoped $LiScP_2O_7:Cr^{3+}$. *Chem. Mater.,* 2020, **32***,* 2430−2439.

(44) S. B. Naghadeh, B. Luo, Y.-C. Pu, Z. Schwartz, W. R. Hollingsworth, S. A. Lindley, A. S. Brewer, A. L. Ayzner and J. Z. Zhang, Size Dependence of Charge Carrier Dynamics in Organometal Halide Perovskite Nanocrystals: Deciphering Radiative Versus Nonradiative Components. *J. Phys. Chem. C.,* 2019, **123**, 4610-4619.

(45) A. Kausar, A. Sattar, C. Xu, S. Zhang, Z. Kang and Y. Zhang, Advent of Alkali Metal Doping: A Roadmap for the Evolution of Perovskite Solar Cells. *Chem. Soc. Rev.,* 2021, **50**, 2696.

(46) J. Duan, Y. Zhao, X. Yang, Y. Wang, B. He and Q. Tang, Lanthanide Ions Doped

$CsPbBr_3$ Halides for HTM-Free 10.14%-Efficiency Inorganic Perovskite Solar Cell with an Ultrahigh Open-Circuit Voltage of 1.594 V. *Adv. Energy Mater.,* 2018, **8**, 1802346.

(47) J. Xu, J.-B. Liu, B.-X. Liu, J. Wang and B. Huang, Defect Engineering of Grain Boundaries in Lead-Free Halide Double Perovskites for Better Optoelectronic Performance. *Adv. Funct. Mater.,* 2019, **29**, 1805870.

(48) W. Zhou, J. Fan, J. Luo, L. Lin, J. Zhou, J. Zhang, Z. Zhu and X. Zhang, Structural Confinement and Energetic Matching Synergistic Effect toward a High-Energy Transfer Efficiency and a Significant Red Emission Enhancement in a Eu^{2+}, Ln^{3+} Co-doped $Sr_9LiMn(PO_4)_7$ Whitlockite Phosphor, *Inorg. Chem.*, 2022, **61**, 8767-8781.

(49) K. Elzbieciak-Piecka, M. Suta and L. Marciniak, Structurally induced tuning of the relative sensitivity of $LaScO_3:Cr^{3+}$ luminescent thermometers by co-doping lanthanide ions, *Chem. Eng. J.,* 2021, **421**, 129757.

(50) Q. Meng, L. Zhou, Q. Pang, X. He, T. Wei and J. Z. Zhang, Enhanced Photoluminescence of All-Inorganic Manganese Halide Perovskite-Analogue Nanocrystals by Lead Ion Incorporation, *J. Phys. Chem. Lett.*, 2021, **12**, 10204-10211.

(51) S. Sarang, W. Delmas, S. Bonabi Naghadeh, V. Cherrette, J. Z. Zhang and S. Ghosh, Low-Temperature Energy Transfer via Self-Trapped Excitons in Mn(2+)-Doped 2D Organometal Halide Perovskites, *J. Phys. Chem. Lett.*, 2020, **11**, 10368-10374.

(52) J.-H. Wei, J.-F. Liao, X.-D. Wang, L. Zhou, Y. Jiang and D.-B. Kuang, All-Inorganic Lead-Free Heterometallic $Cs_4MnBi_2Cl_{12}$ Perovskite Single Crystal with

Highly Efficient Orange Emission, *Matter*, 2020, **3**, 892-903.

(53) T. Cai, J. Wang, W. Li, K. Hills-Kimball, H. Yang, Y. Nagaoka, Y. Yuan, R. Zia and O. Chen, Mn^{2+}/Yb^{3+} Codoped $CsPbCl_3$ Perovskite Nanocrystals with Triple-Wavelength Emission for Luminescent Solar Concentrators, *Adv. Sci.*, 2020, **7**, 2001317.

(54) J. Luo, X. Wang, S. Li, J. Liu, Y. Guo, G. Niu, L. Yao, Y. Fu, L. Gao, Q. Dong, C. Zhao, M. Leng, F. Ma, W. Liang, L. Wang, S. Jin, J. Han, L. Zhang, J. Etheridge, J. Wang, Y. Yan, E. H. Sargent and J. Tang, Efficient and stable emission of warm-white light from lead-free halide double perovskites, *Nature*, 2018, **563**, 541-545.

(55) D. Wu, L. Liu, H. Liang, H. Duan, W. Nie, J. Wang, J. Peng and X. Ye, $LiBAlF_6:Cr^{3+}$ (B = Ca, Sr) Fluoride Phosphors with Ultra-broad Near-infrared Emission for NIR pc-LEDs. *Ceram. Int.,* 2022, **48**, 387-396.

(56) X. Li, Y. Wu, S. Zhang, B. Cai, Y. Gu, J. Song and H. Zeng, $CsPbX_3$ Quantum Dots for Lighting and Displays: Room-Temperature Synthesis, Photoluminescence Superiorities, Underlying Origins and White Light-Emitting Diodes, *Adv. Funct. Mater.*, 2016, **26**, 2435-2445.

(57) H. Yu, J. Chen, R. Mi, J. Yang, Y.-g. Liu, Broadband Near-infrared Emission of $K_3ScF_6:Cr^{3+}$ Phosphors for Night Vision Iimaging System Sources. *Chem. Eng. J.,* 2021, **417**, 129271.